



Nonlinear optical response of twisted bilayer grapheneJ. W. Zuber and C. Zhang *School of Physics and Institute for Superconducting and Electronic Materials, University of Wollongong, New South Wales 2522, Australia* (Received 9 April 2021; revised 4 June 2021; accepted 4 June 2021; published 14 June 2021)

Twisted bilayer graphene (TBG) exhibits many fascinating electronic and transport properties. Here we analyze the nonlinear optical response in TBG in the terahertz regime. By considering an effective two-band model with a simplified interlayer tunnel, we write the time-dependent wave function in terms of generalized Floquet states consisting of multiple high-order harmonics. A two-component spinor recursion relation is solved up to terms in the third order of the applied field. The third-order conductivity of TBG with different twist angles is obtained. For small twist angles the Kerr effect dominates over the high harmonic processes, while for large twist angles, the high harmonic processes completely dominate the nonlinear response. We attribute this phenomenon to the band dispersion sensitive transition probability in low- and high-energy regimes. The frequency- and temperature-dependent critical field is also presented. The critical field is insensitive to the temperature, indicating that the nonlinear response persists at room temperature.

DOI: [10.1103/PhysRevB.103.245417](https://doi.org/10.1103/PhysRevB.103.245417)**I. INTRODUCTION**

The advancements in fabrication of atomically thin materials have provided a catalyst for the theoretical and experimental study of new two-dimensional superlattice materials in which the orientations of the sublattices are purposely misoriented [1–5]. Owing to the diverse range of exciting properties found in single-layer graphene (SLG), such as universal optical conductance [6–9], the half-integer quantum Hall effect [4,10,11], strong suppression of weak localization [12,13], magnetic enhancement of optical conductivity [14], and a strong nonlinear response in the terahertz (THz) regime [15,16], bilayer graphene (BLG) structures have been the focus of intense research [17–21]. Within the framework of BLG, interlayer interactions have been experimentally shown to play a crucial role in determining the electronic properties [22–25]. As such many stacking orientations have been studied theoretically and fabricated experimentally, including AB (Bernal-inequivalent lattice sites are the opposite in the top and bottom layers), AA (inequivalent lattice sites match each other in the top and bottom layers), and ABC (trilayer) graphene bilayers [26]. However, the most intriguing BLG structure, and the focus of our study, is so-called twisted bilayer graphene (TBG). In TBG, the two graphene sheets are stacked at an arbitrary angle θ to one another (see Fig. 1), making AA ($\theta = 0^\circ$) and AB ($\theta = 60^\circ$) special cases of TBG.

The interaction between misoriented layers in TBG provides rich and novel electronic properties, distinct from those seen in the Dirac setting of SLG. Of particular interest are the spectral properties of TBG for small twist angles, including the opening of band gaps, creation of a Van Hove singularity, and significantly reduced band velocity near the Dirac point [5,27–30]. These dispersion properties have been verified experimentally via numerous spectroscopy methods such as Raman spectroscopy [31–33], angle-resolved pho-

toemission spectroscopy [34], optical reflection spectroscopy [35], and terahertz time domain spectroscopy [36]. A plethora of intriguing properties have since been shown to result from the electronic structure of TBG, including, but not limited to, the anomalous Hall effect [37,38], plasmon resonance [39], circular dichroism [40], the chiral response [41,42], topologically protected zero modes [43], Mott insulating and superconductivity [44], the THz photogalvanic response [45,46], exotic Landau levels [43,47,48], and Kerr effects [37,48]. TBG has even been studied for use in gratings and metasurfaces [42,49,50].

The property we are most interested in is the optical nonlinear response of TBG. There have been numerous studies of the linear optical response of TBG [17,39–41,51,52] which revealed a strong optical response (up to 8 times that of SLG under equivalent conditions), physically rich optical selection rules depending on the crystalline symmetries, and Landau levels strongly dependent on twist angle. Such studies have been verified experimentally and computationally [36,53]. However, the nonlinear optical response of TBG is still largely unstudied. Studies on the nonlinear optical response of Bernal BLG [18,54] revealed a strong nonlinear effect in the THz to far-infrared (FIR) region where for very moderate electric fields of 1000 V/cm the nonlinear conductivity becomes relevant and at room temperature a frequency-tripling term can be induced. A recent computational nonperturbative model by Ikeda [55] revealed appreciable higher-order harmonics (up to the eighth order) exist in TBG with fixed $\theta = 21.79^\circ$ in the near- to mid-infrared (NIR-MIR) region. Since the higher-order harmonics are not attributed to Dirac-like carriers, but rather interlayer couplings, these harmonics are not seen in SLG or BLG. Inspired by these conclusions and recent evidence of the nonlinear activity of TBG through other properties such as Kerr rotation [37], nonlinear Hall effects [37,56], second harmonic generation [57], Rabi

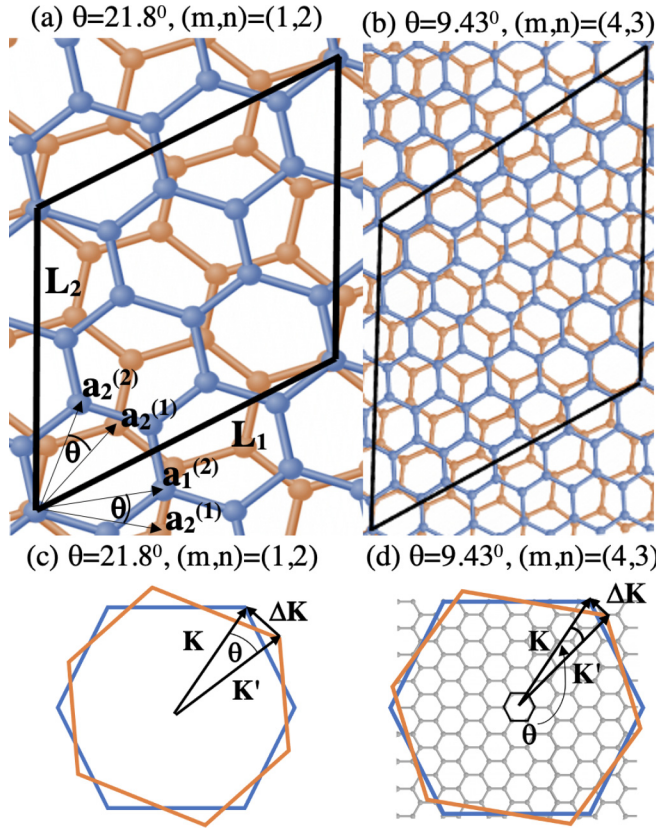


FIG. 1. (a) and (b) show the unit cells of TBG (spanned by \mathbf{L}_1 and \mathbf{L}_2), the top layer (spanned by $\mathbf{a}_1^{(2)}$ and $\mathbf{a}_2^{(2)}$), and the bottom layer (spanned by $\mathbf{a}_1^{(1)}$ and $\mathbf{a}_2^{(1)}$) at different twist angles. The blue lattice represents the top layer (layer 2), and the orange lattice represents the bottom layer (layer 1). (c) and (d) show the first Brillouin zones of each layer. The first Brillouin zone of TBG is defined by \mathbf{K} and \mathbf{K}' , which come from the \mathbf{K} points of the top and bottom layers, respectively. The solid black hexagon in (d) represents the “folded-back” Brillouin zone of TBG.

oscillations [58], and circular dichroism [40] we proceed to survey the nonlinear optical response of TBG in the THz-FIR region.

To study the nonlinear optical response we adopt a quantum mechanical model which couples the carriers (electrons) to a time-dependent electric field. By expanding electronic states in successive orders of the electric field we can obtain arbitrary-order nonlinear wave functions. Furthermore, we can identify unique electron-photon processes for each order wave function by grouping together different frequency harmonics. The current response for any order wave function is straightforwardly calculated, and the sensitivity to the temperature, Fermi level, direction of the field, and twist angle may be surveyed.

II. THEORY

A. Atomic structure and Brillouin zone

In reference to Fig. 1 the structure of TBG may be characterized by a single twist parameter $0^\circ \leq \theta \leq 30^\circ$ since rotation by $60^\circ - \theta$ is equivalent to rotation by $-\theta$ followed by a translation of the second layer [59,60]. Some studies

also include such a translation parameter δ in which the top (or bottom) layer is moved in the xy plane relative to the other [53,61]. We fix $\delta = 0$ from the outset. Since AB stacked BLG is difficult to fabricate thanks to disorders introduced by substrates, our coordinate frame is chosen so that $\theta = 0$, the system is AA stacked, and the lattice vectors for both layers are $\mathbf{a}_1 = a(1, 0)$ and $\mathbf{a}_2 = a(1/2, \sqrt{3}/2)$, where $a \approx 0.246$ nm is the lattice constant. When $\theta \neq 0$, we rotate each layer $\theta/2$ in different directions around a common B site so that the lattice vectors of the individual layers are

$$\begin{aligned} \mathbf{a}_1^{(1)} &= a[\cos(\theta/2), -\sin(\theta/2)] \\ \mathbf{a}_2^{(1)} &= a[\cos(\pi/3 - \theta/2), \sin(\pi/3 - \theta/2)] \\ \mathbf{a}_1^{(2)} &= a[\cos(\theta/2), \sin(\theta/2)] \\ \mathbf{a}_2^{(2)} &= a[\cos(\pi/3 + \theta/2), \sin(\pi/3 + \theta/2)]. \end{aligned} \quad (1)$$

Using (1), we can determine the Brillouin zones (BZs) of each layer and hence the vector connecting their \mathbf{K} points for any θ ,

$$\Delta\mathbf{K} = \mathbf{K}^{(2)} - \mathbf{K}^{(1)} = \frac{2\pi \sin(\theta/2)}{\sqrt{3}a}(\sqrt{3}, -1). \quad (2)$$

Although the TBG lattice is not generally periodic for any twist angle, for some specific twist angles the two periods happen to match, allowing us to rigorously define a lattice constant L and BZ for TBG. Such angles occur when two general lattice vectors (spanned by $\mathbf{a}_i^{(j)} : i, j = 1, 2$) from each layer are equal,

$$\begin{aligned} m\mathbf{a}_1^{(1)} + n\mathbf{a}_2^{(1)} &= m\mathbf{a}_1^{(2)} + n\mathbf{a}_2^{(2)} \\ \Rightarrow \cos\theta &= \frac{m^2 + n^2 + 4mn}{2(m^2 + n^2 + mn)}. \end{aligned} \quad (3)$$

The lattice constant L is then determined by

$$L = |m\mathbf{a}_1^{(1)} + n\mathbf{a}_2^{(1)}| = \frac{a|m - n|}{2 \sin(\theta/2)}, \quad (4)$$

with the TBG lattice vectors

$$\begin{aligned} \mathbf{L}_1 &= (\sqrt{3}L/2, L/2), \\ \mathbf{L}_2 &= (0, L). \end{aligned} \quad (5)$$

Using the lattice vectors in (5), we can analytically calculate the BZ as

$$\begin{aligned} [\text{BZ}] &= \left\{ (k_x, k_y) \in \mathbb{R}^2 : |k_y| \leq \frac{\pi}{\sqrt{3}L} \cap |k_y + \sqrt{3}k_x| \right. \\ &\quad \left. \leq \frac{2\pi}{L} \cap |k_y - \sqrt{3}k_x| \leq \frac{2\pi}{L} \right\}. \end{aligned} \quad (6)$$

Consistent with Figs. 1(a) and 1(b) the \mathbf{k} -space BZ in (6) grows $\propto L^{-1}$ for larger twist angles corresponding to the increased unit cell size in position space for smaller twist angles. Despite the difference in area, each BZ of TBG can be folded back into a central hexagonal region, as shown in Fig. 1(d), where the $\mathbf{K}^{(i)}$ points are translated to $\mathbf{K}^{(1)} \rightarrow \mathbf{K}'$, $\mathbf{K}^{(2)} \rightarrow \mathbf{K}$, $\mathbf{K}'^{(1)} \rightarrow \mathbf{K}$, $\mathbf{K}'^{(2)} \rightarrow \mathbf{K}'$ [53,62]. This procedure shows (2) represents the vector connecting the \mathbf{K} and \mathbf{K}' points in TBG.

B. Electronic and topological properties

The most popular model for describing the electronic structure of BLG is given by the 4×4 Hamiltonian [43,47,51,63],

$$H(\mathbf{k}) = \begin{pmatrix} H_G(\mathbf{k} + \Delta\mathbf{K}/2) & \sum_{i=-1}^1 (H_{\perp}^i) \\ \sum_{i=-1}^1 (H_{\perp}^i)^{\dagger} & H_G(\mathbf{k} - \Delta\mathbf{K}/2) \end{pmatrix}, \quad (7)$$

where

$$H_G(\mathbf{k}) = v_F \hbar \begin{pmatrix} 0 & k_x - ik_y \\ k_x + ik_y & 0 \end{pmatrix}$$

is the SLG Hamiltonian, $v_F \approx 3 \times 10^5$ m/s is the Fermi velocity [18,28,47],

$$H_{\perp}^0 = t \begin{pmatrix} 1 & 1 \\ 1 & 1 \end{pmatrix}, \quad H_{\perp}^{\pm 1} = t \begin{pmatrix} e^{\mp i2\pi/3} & 1 \\ e^{\pm i2\pi/3} & e^{\mp i2\pi/3} \end{pmatrix}$$

$$\epsilon_{s,m} = s \sqrt{9t^2 + (\epsilon_G^+)^2 + (\epsilon_G^-)^2 + m \sqrt{[9t^2 + (\epsilon_G^+)^2 + (\epsilon_G^-)^2]^2 - 4(\epsilon_G^+)^2(\epsilon_G^-)^2}}, \quad (8)$$

where $(s, m) = \pm 1$ denote the bands and

$$\epsilon_G^{\pm} = v_F \hbar \sqrt{(k_x \pm \Delta K_x/2)^2 + (k_y \pm \Delta K_y/2)^2}.$$

The Hamiltonian in (7) may be reduced to an effective two-band model in the low-energy limit $t \gg v_F \hbar \Delta K$, which is valid for the twist angles $3^\circ \leq \theta \leq 10^\circ$ discussed in this work. To establish the two-band model we first assume a simplified version of the interlayer coupling term

$$\sum_{i=-1}^1 H_{\perp}^i \rightarrow 3 \times \frac{5}{2} t \begin{pmatrix} 0 & 0 \\ 1 & 0 \end{pmatrix},$$

where the factor of $\frac{5}{2}$ is introduced to match the Bernal-stacked ($\theta = 0$) spectrum [47]. In the eigenbasis $\{\psi^1, \psi^2, \psi_{\theta}^1, \psi_{\theta}^2\}$ where (1,2) belong to the bottom layer and $(1_{\theta}, 2_{\theta})$ belong to the twisted bottom layer, the time-independent Schrödinger equation (TISE) reads

$$\begin{aligned} v_F(k_x + ik_y + \Delta K_x/2 + i\Delta K_y/2)^* \psi^2 &= E \psi^1, \\ v_F(k_x + ik_y + \Delta K_x/2 + i\Delta K_y/2) \psi^1 + \tilde{t} \psi_{\theta}^1 &= E \psi^2, \\ \tilde{t} \psi^2 + v_F(k_x + ik_y - \Delta K_x/2 - i\Delta K_y/2)^* \psi_{\theta}^2 &= E \psi_{\theta}^1, \\ v_F(k_x + ik_y - \Delta K_x/2 - i\Delta K_y/2) \psi_{\theta}^1 &= E \psi_{\theta}^2, \end{aligned} \quad (9)$$

where $\tilde{t} = \frac{15}{2} t$. With (9) we observe that the zero-energy solutions are spanned by ψ^1 and ψ_{θ}^2 and the other basis vectors, ψ^2 and ψ_{θ}^1 , are strongly hybridized by the hopping parameter \tilde{t} . Since we seek low-energy solutions, we can neglect

$$\begin{aligned} E \psi^2 &\approx 0, \\ E \psi_{\theta}^1 &\approx 0. \end{aligned}$$

The effective two-band Hamiltonian can be written as [43,47,63]

$$H_{2,\text{Band}}(\mathbf{k}) = -\frac{v_F^2 \hbar^2}{\tilde{t}} \begin{pmatrix} 0 & q^{\dagger}(\mathbf{k}) \\ q(\mathbf{k}) & 0 \end{pmatrix}, \quad (10)$$

are the three lowest-order Fourier components of the hopping matrix between the two layers, which are dominant for small twist angles $3^\circ \leq \theta \leq 10^\circ$ [47,51], and t is a hopping parameter which generally depends on θ but may be taken to be constant and ≈ 150 meV [24,43,64] for the region of small twist angles considered here. It should be noted that this model neglects commensuration effects between the two layers. Although these effects are minor since coupling between Dirac cones is negligible [59,65,66], in reality commensuration effects restrict the BZ to a small degree.

The model described by (7) is a continuum limit around a single pair of \mathbf{K} points (\mathbf{K}, \mathbf{K}'); as such, when discussing symmetries, we do not refer to the lattice symmetries, but rather to those of its energy bands,

where $q(\mathbf{k}) = (k_x + ik_y)^2 - (\Delta K_x/2 + i\Delta K_y/2)^2 := k^2 + (\Delta K/2)^2$. The associated dispersion relation is

$$\epsilon_s = s \frac{v_F^2 \hbar^2}{\tilde{t}} |q(\mathbf{k})| = s \frac{v_F^2 \hbar^2}{\tilde{t}} \epsilon_G^+ \epsilon_G^-. \quad (11)$$

The dispersion relation is plotted in Fig. 2. The most salient features of the TBG dispersion are evidently captured in the saddle point at $\mathbf{k} = 0$, logarithmic Van Hove singularity corresponding to the Dirac points at $\pm \Delta \mathbf{K}$ (one from each layer), and the overall anisotropy owing to $\Delta K_x \neq \Delta K_y$. From the low-energy expansion of (10) around $\pm \Delta \mathbf{K}$, we observe that electrons with fixed energy at \mathbf{K} have the same chirality as equivalent energy carriers at \mathbf{K}' . Hence, electrons at either $\mathbf{K}^{(\prime)}$ point will experience a Berry phase of $\gamma = (\pm)\pi$ on a closed orbit around that Dirac point. Moreover, collapsing the Dirac points, $\Delta \mathbf{K} = 0$ need not be accompanied by a gap

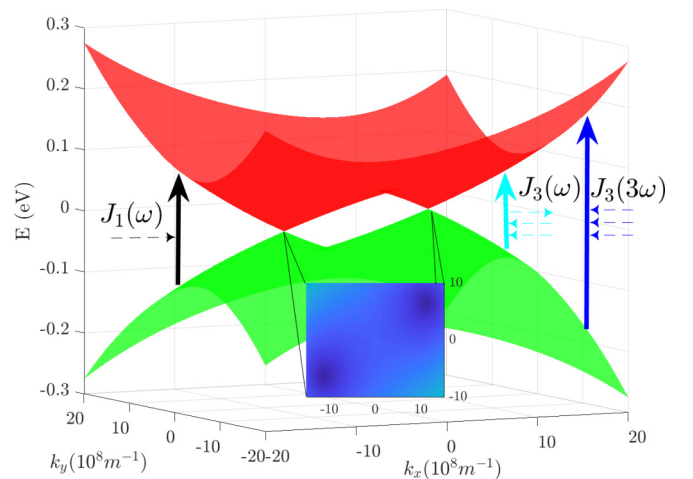


FIG. 2. Dispersion relation for the effective two-band model of TBG with $\theta \approx 5^\circ$. The pop-out shows the two Dirac points at $\pm \Delta \mathbf{K}$, while the arrows depict the single-photon current and two different three-photon contributions to the third-order current.

opening (Van Hove singularity). In view of these topological properties $H_{2\text{Band}}$ may be viewed as a representative of the topological universality class that also includes H , respecting the same representation of inversion symmetry $H(-\mathbf{k}) = -H(\mathbf{k})^* [E(\mathbf{k}) \rightarrow -E(-\mathbf{k})]$.

$$H_{2\text{Band}}(\mathbf{k}, \mathbf{A}) = -\frac{v_F^2 \hbar^2}{\tilde{t}} \begin{pmatrix} 0 & q^* + \frac{2eE}{i\hbar\omega} k^* e^{i\omega t} - \frac{e^2 E^2}{\hbar^2 \omega^2} e^{2i\omega t} \\ q + \frac{2eE}{i\hbar\omega} k e^{i\omega t} - \frac{e^2 E^2}{\hbar^2 \omega^2} e^{2i\omega t} & 0 \end{pmatrix}. \quad (12)$$

Now we assume that the time-dependent wave function is given in the form of generalized Floquet states,

$$\psi(\mathbf{k}, t) = \sum_{n=0}^{\infty} \phi_n(\mathbf{k}) e^{in\omega t} e^{-i\epsilon t/\hbar}, \quad (13)$$

where $\epsilon = |\epsilon_s|$ and the two-component spinor $\phi_n(\mathbf{k}) = (\alpha_n(\mathbf{k}), \beta_n(\mathbf{k}))^T$. Substituting (13) into the TISE yields

$$\hbar \sum_{n=0}^{\infty} (\epsilon/\hbar - n\omega) \phi_n(\mathbf{k}) e^{i(n\omega - \epsilon/\hbar)t} = - \sum_{n=0}^{\infty} e^{i(n\omega - \epsilon/\hbar)t} \frac{v_F^2 \hbar^2}{\tilde{t}} \begin{pmatrix} 0 & q^* + \frac{2eE}{i\hbar\omega} k^* e^{i\omega t} - \frac{e^2 E^2}{\hbar^2 \omega^2} e^{2i\omega t} \\ q + \frac{2eE}{i\hbar\omega} k e^{i\omega t} - \frac{e^2 E^2}{\hbar^2 \omega^2} e^{2i\omega t} & 0 \end{pmatrix}.$$

The TISE above contains information on all-order multiple photon processes in TBG. Owing to the orthonormality of $e^{i\omega t}$, we can isolate each order through the two-level recurrence relations for the spinor components

$$\begin{aligned} \tilde{t}(\epsilon - n\hbar\omega)\alpha_n &= -v_F^2 \left(\beta_n q^* + \frac{2eE}{i\hbar\omega} k^* \beta_{n-1} - \frac{e^2 E^2}{\hbar^2 \omega^2} \beta_{n-2} \right), \\ \tilde{t}(\epsilon - n\hbar\omega)\beta_n &= -v_F^2 \left(\alpha_n q + \frac{2eE}{i\hbar\omega} k \alpha_{n-1} - \frac{e^2 E^2}{\hbar^2 \omega^2} \alpha_{n-2} \right). \end{aligned} \quad (14)$$

From the solutions to (14) we can calculate the n th-order total current using the relation

$$J_v^n = \frac{e}{4\pi^2} \int_{[\text{BZ}]} d^2\mathbf{k} N_F(\mu, \epsilon) (\psi_m^\dagger v_v \psi_{m'}), \quad (15)$$

where [BZ] is the BZ in (6),

$$\begin{aligned} N_F(\mu, \epsilon) &= n_F(\mu, -\epsilon) - n_F(\mu, \epsilon) \\ &= \frac{\sinh(\epsilon/k_B T)}{\cosh(\mu/k_B T) + \cosh(\epsilon/k_B T)} \end{aligned}$$

is the interband distribution function, $v_v = \hbar^{-1} \partial_{k_v} H_{2\text{Band}}$ is the velocity operator in the direction $v = x, y$, and indices $m, m' \in \mathbb{Z}$ have the restriction $m + m' = n$. The time-averaged observable part of the current in each direction is given by

$$\text{Re}\{J_x^n\} = -\frac{ev_F^2 \hbar}{\pi^2 \tilde{t}} \int_{[\text{BZ}]} d^2\mathbf{k} N_F \text{Re} \left\{ k \sum_{n'=0}^n \alpha_{n'}^* \beta_{n-n'} \right\} \quad (16)$$

and

$$\text{Re}\{J_y^n\} = \frac{ev_F^2 \hbar}{\pi^2 \tilde{t}} \int_{[\text{BZ}]} d^2\mathbf{k} N_F \text{Im} \left\{ k \sum_{n'=0}^n \alpha_{n'}^* \beta_{n-n'} \right\}. \quad (17)$$

Note that since we seek the real part of the spinor sum, each $\alpha_{n'}^* \beta_{n-n'}$ is interchangeable with its complex conjugate. Hence, when isolating oscillatory terms, both $\alpha_{n'}^* \beta_{n-n'}$ and

C. Nonlinear conductivity

Consider a system subject to a spatially constant, time-dependent optical field along the x axis described by $\mathbf{E} = E e^{i\omega t} \hat{x}$. It yields a vector potential $\mathbf{A} = -\frac{E}{i\hbar\omega} e^{-i\omega t} \hat{x}$, so that under Pierel's substitutions ($e > 0$) the Hamiltonian becomes

$\alpha_{n-n'}^* \beta_{n'}$ are $\propto e^{i|n-2n'|\omega t}$. In this view (16) and (17) will contain only one term oscillating with frequency 1ω for $n = 1$ and two terms, one oscillating with frequency 1ω and another oscillating with frequency-tripled term, for $n = 3$, as per Fig. 2. When discussing nonlinear conductivities herein, we define the n th-order conductivity $\sigma_v^{(n)}$ from (15) by

$$J_v^n = \sigma_v^{(n)} E^n$$

for $v = x, y$.

III. RESULTS

For the parameters discussed in the previous section, the minimum of the $\epsilon_{1,1}$ band in the four-band model ranges from 0.78 eV for $(m, n) = (4, 3) \Rightarrow \theta = 9.43^\circ$ to 0.34 eV for $(m, n) = (11, 10) \Rightarrow \theta = 3.15^\circ$. Hence, for our effective two-band model to remain valid we should sample only fields for which $\hbar\omega + \mu < 0.34 \text{ eV} \Rightarrow \omega < 2.13 \times 10^{14} \text{ Hz}$. Terahertz frequencies adhere well to this restriction and are the focus of this paper.

In the absence of an electric field only the $n = 0$ terms contribute, and the solution to (14) is

$$\phi_0(\mathbf{k}) = \frac{1}{\sqrt{2}} \begin{pmatrix} -v_F^2 \hbar^2 q^* / (\tilde{t}\epsilon) \\ 1 \end{pmatrix}. \quad (18)$$

Substituting (18) into (16) or (17) yields no current as there must be a nonzero electric field for a nonzero current.

A. First-order conductivity

Substituting (18) into (16) results in $\text{Re}(J_x^{(0)}) = 0$, as one would expect. The single-photon processes are described by the spinor

$$\phi_1(\mathbf{k}) = \frac{\sqrt{2}eE}{i(\hbar\omega)^2(2\epsilon - \hbar\omega)} \begin{pmatrix} v_F^2 \hbar^2 \tilde{t}^{-1} (2\epsilon k_x - k\hbar\omega) \\ -\epsilon(q^*)^{-1} (2\epsilon k_x - k^* \hbar\omega) \end{pmatrix}. \quad (19)$$

The simplest analytic expression for $\text{Re}(J_x^{(1)})$ is obtained by substituting (19) into (16) and using the Sokhotski-Plemelj relations to yield

$$\text{Re}\{J_x^{(1)}\} = -\frac{4eEv_F^8\hbar^7}{\tilde{t}^4\pi^2} \int_{|\text{BZ}|} d^2\mathbf{k} \frac{N_F}{(\hbar\omega\epsilon)^2} \left[\begin{aligned} & -K_x K_y [2\epsilon k_x^2 - \hbar\omega(k_x^2 + k_y^2)] (k_x^2 + k_y^2 - K_x^2 + K_y^2) (2\epsilon - \hbar\omega)^{-1} \\ & + \left([2\epsilon k_x^2 - \hbar\omega(k_x^2 + k_y^2)] (k_x^2 k_y^2 + K_x^2 K_y^2) \right. \\ & \quad \left. + \epsilon k_x^2 k_y^2 (k_x^2 - k_y^2 - K_x^2 + K_y^2) \right) 2\pi \delta(2\epsilon - \hbar\omega) \end{aligned} \right], \quad (20)$$

where $K_v = \Delta K_v/2$ for short. The Sokhotski-Plemelj relations allow us to separate a diffuse part of the current $\propto (2\epsilon - \hbar\omega)$ [top line in (20)] and a harmonic part $\propto \delta(2\epsilon - \hbar\omega)$. The diffuse part is not present in SLG. Numerically, the δ functions are approximated using the Lorentzian representation $\delta(x) \rightarrow (\nu/\pi)/(x^2 + \nu^2)$, where $\nu = 7$ meV is the broadening parameter [51]. The first-order conductivity $\sigma_x^{(1)} = \text{Re}(J_x^{(1)})/E$ scaled by $\sigma_0^{(1)} = e^2/4\hbar$ is plotted as a function of frequency for different twist angles, temperatures, and Fermi levels in Fig. 3. In terms of frequency dependence, unlike SLG, TBG has no universal conductivity and instead decreases approximately as $\propto \omega^{-2}$ using the low-energy effective two-band model. This was observed previously in the lower limit of previous optical conductivity studies in the MIR-NIR range [51,55]. The first-order conductivity magnitude of TBG was previously reported to vary between $0.4\sigma_0^{(1)}$ and $1.5\sigma_0^{(1)}$ in the THz region [17,39,40,51] for intermediate twist angles $\theta \approx 5^\circ$. Our results lie within this region of validity.

Figure 3(a) shows the most striking result of the first-order conductivity. By changing the twist angle only a few degrees the conductivity is altered by up to an order of magnitude. This sensitivity is defined by two competing factors. First, the BZ is enlarged almost twofold when increasing $\theta = 3.15^\circ \rightarrow 9.43^\circ$, encapsulating the influence of a broader spectrum of carriers leading to an increased conductivity. Second, from a dispersion perspective, the saddle point is lowered for smaller twist angles, as is the gradient of the bands at larger \mathbf{k} . Since a lower saddle point enhances interband conductivity (carriers transitioning between \mathbf{K} and \mathbf{K}') and the spectral regions around each $\mathbf{K}^{(\prime)}$ point are broadened by a lower Fermi velocity,

one should expect an increase in conductivity. Evidently, the BZ expansion is the dominant mechanism for our chosen parameters, saturating the dispersion effects, leading to an exponential increase in first-order conductivity with twist angle.

The dependences shown in Figs. 3(b) and 3(c) are both completely defined by the distribution function N_F . As $\mu \rightarrow 0$, the term $\cosh(\mu/k_B T)$ decreases towards 1, increasing N_F and the overall conductivity. Physically, this may be attributed to Pauli blocking mitigating the interband contribution of deep carriers, increasing the chemical potential, leading to a reduced phase space for the final states, a process not present in the intraband response of SLG where $\sigma^{(1)}$ increases $\propto \ln[2 \cosh(\mu/2T)]$, in accordance with the Boltzmann-Drude expression. Similarly, there is an approximately twofold increase in conductivity when lowering the temperature from 300 to 0 K, mirroring what is observed in SLG using the same technique[16]. The anisotropy of the first-order conductivity is surveyed in Fig. 4. These data are obtained by using $\mathbf{E} = E e^{i\omega t} \hat{y}$, following the same steps to calculate ϕ_n and numerically evaluating (17). One observes first that TBG is a better linear conductor in the y direction of our coordinate system, following directly from $\Delta K_y < \Delta K_x$, allowing interlayer carriers to move between \mathbf{K} and $\mathbf{K}_{(\theta)}$ more freely. Furthermore, anisotropy is larger for smaller twist angles since the lower saddle point also enhances interlayer conductivity. Both of these features are very robust to THz frequency, with the dominance of J_y shown to persist for frequencies into the NIR region for fields as high as 3.2 MV/cm [55]. The anisotropy is not sensitive to temperature or Fermi level since the distribution function is not sensitive to field direction.

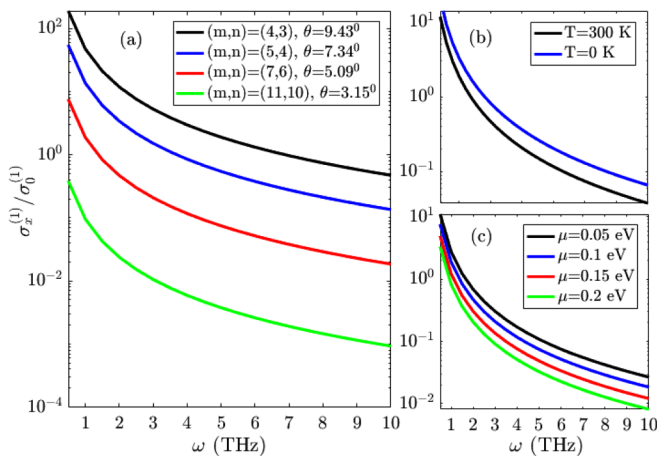


FIG. 3. First-order conductivity $\sigma_x^{(1)}$ in the THz region with different (a) twist angles, (b) temperatures, and (c) Fermi levels. Unless otherwise stated, the parameters are $(m, n) = (7, 6)$, $T = 300$ K, and $\mu = 0.1$ eV.

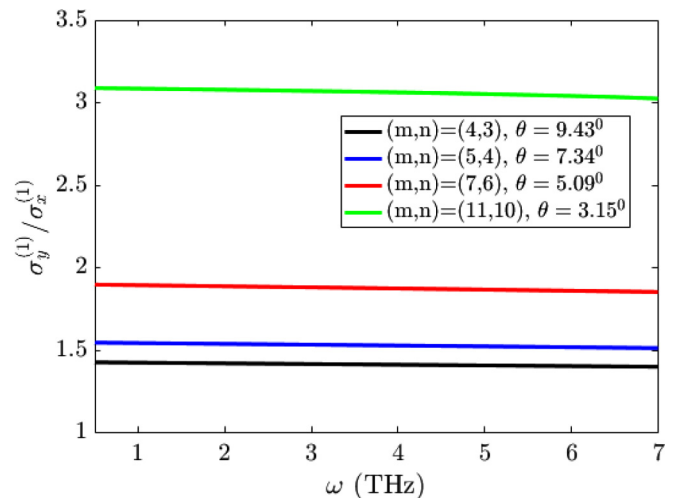


FIG. 4. Anisotropy of the first-order conductivity for $T = 300$ K and $\mu = 0.1$ eV.

B. Third-order conductivity

Consistent with the compound inversion plus time-reversal symmetry of the system, we find that $\sigma_y^{(2n)} = 0 \forall n \in \mathbb{Z}$ [18,67–69]. Hence, the lowest-order nonlinear contribution to the current response will be the third order. The third-order solution to (14) yields the spinor

$$\phi_3(\mathbf{k}) = \frac{v_F^2 \hbar^2 e^3 E^3}{i3(\hbar\omega)^5 \tilde{t}^2 (2\epsilon - 3\hbar\omega)} \left[\begin{aligned} & \frac{8v_F^8 \hbar^8 \left(\begin{aligned} & k^* q \epsilon (2\epsilon k_x - k^* \hbar\omega) [(\epsilon - 2\hbar\omega)(k^* q + kq^*) - \hbar\omega k^* q] \\ & + kq^* (2\epsilon k_x - k\hbar\omega) [\epsilon^2 (kq^* + k^* q) - \hbar\omega (5\epsilon - 6\hbar\omega) k^* q] \end{aligned} \right)}{4\sqrt{2}\tilde{t}^3 \epsilon^2 \hbar\omega (2\epsilon - \hbar\omega)(\epsilon - \hbar\omega)} \\ & + \frac{2\epsilon \{k\epsilon [\epsilon \tilde{t}^2 (\epsilon - 2\hbar\omega) + v_F^4 \hbar^4 (q^*)^2] + k^* (\epsilon - 3\hbar\omega) [\epsilon \tilde{t}^2 (\epsilon - \hbar\omega) + v_F^4 \hbar^4 q^2]\}}{4\sqrt{2}\tilde{t}\epsilon q (\epsilon - \hbar\omega)} \\ & + \frac{\sqrt{2}v_F^4 \hbar^4 [(2\epsilon k_x - k\hbar\omega)\epsilon q^* - (2\epsilon k_x - k^* \hbar\omega)(\epsilon - 3\hbar\omega)q]}{\tilde{t}\epsilon (2\epsilon - \hbar\omega)}, \\ & \frac{8v_F^6 \hbar^6 \left(\begin{aligned} & \epsilon^3 \tilde{t}^2 k (2\epsilon k_x - k\hbar\omega) [(\epsilon - 2\hbar\omega)(k^* q + kq^*) - \hbar\omega k^* q^*] \\ & + k^* q^2 v_F^4 \hbar^4 (2\epsilon k_x - k^* \hbar\omega) [\epsilon^2 (kq^* + k^* q) - \hbar\omega (5\epsilon - 6\hbar\omega) kq^*] \end{aligned} \right)}{4\sqrt{2}\tilde{t}^4 \epsilon^3 \hbar\omega (2\epsilon - \hbar\omega)(\epsilon - \hbar\omega)} \\ & - \frac{2v_F^2 \hbar^2 \{k^* \epsilon [\epsilon \tilde{t}^2 (\epsilon - \hbar\omega) + v_F^4 \hbar^4 q^2] + k(\epsilon - 3\hbar\omega) [\epsilon \tilde{t}^2 (\epsilon - 2\hbar\omega) + v_F^4 \hbar^4 (q^*)^2]\}}{4\sqrt{2}\tilde{t}^2 q (\epsilon - \hbar\omega)} \\ & + \frac{\sqrt{2}v_F^2 \hbar^2 [(2\epsilon k_x - k^* \hbar\omega)\epsilon q - (2\epsilon k_x - k\hbar\omega)(\epsilon - 3\hbar\omega)q^*]}{q^* (2\epsilon - \hbar\omega)} \end{aligned} \right]. \quad (21)$$

We find that the third-order conductivity scales with frequency as ω^{-6} , a drop off two orders of magnitude sharper when compared to SLG [16] and one order sharper than BLG [18] over an equivalent frequency range. Physically, this sharper drop off corresponds to the twist-induced saddle point disproportionately blocking higher-order electron-photon processes and is seen at NIR frequencies where the harmonic bandwidth is reduced for higher orders [55]. As in most systems the high-frequency conductivity will then be dominated by the linear conductivity. Figure 5 shows that in the region $\omega \in [1, 3]$ THz, for a temperature of 300 K and electric field of 10^5 V/m, $\sigma_x^{(3)} E^2 \in [4.32 \times 10^{-8}, 5.75 \times 10^{-3}] \sigma_0^{(1)}$. Under the same parameters for BLG $\sigma_x^{(3)} E^2 \in [6 \times 10^{-3}, 6 \times 10^{-1}] \sigma_0^{(1)}$, showing that TBG exhibits an appreciably smaller nonlinear response due to the $\Delta\mathbf{K} \neq 0$ Van Hove singular-

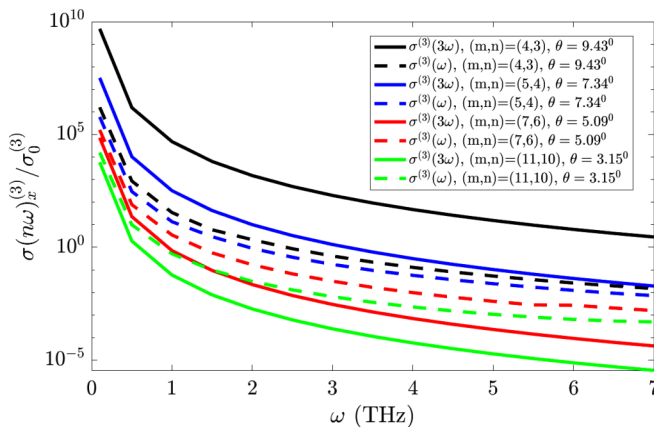


FIG. 5. Third-order conductivity $\sigma_x^{(3)}$ in the THz region for different twist angles with $T = 300$ K, $\mu = 0.1$ eV, and $\sigma_0^{(3)} = e^4 v_F \tilde{t}^{-3} \text{A m}^2/\text{V}^3$.

ity minimizing the spectral weight in the vicinity of $\mathbf{k} = 0$. Furthermore, we observe that for larger twist angles the frequency-tripled portion of the third-order conductivity $\sigma_x^{(3)}(3\omega)$ can be dominant over $\sigma^{(3)}(\omega)$ even at higher THz frequencies. This feature is caused by the increased sensitivity of $\sigma^{(3)}(3\omega)$ to the twist angle as the decreased BZ for smaller θ inhibits the higher transition energy three-photon absorption processes more drastically than the two-photon absorption, one-photon emission process $\sigma^{(3)}(\omega)$. This is in direct contrast to both SLG and BLG, where $\sigma^{(3)}(\omega)$ remains dominant at THz frequencies [16,18].

The anisotropy of the nonlinear response is more feature rich than its linear counterpart. Figure 6 shows a marked difference between the anisotropies of $\sigma^{(3)}(3\omega)$ and $\sigma^{(3)}(\omega)$. The dominance of $\sigma_y^{(3)}(\omega)$ is far more pronounced at lower frequencies owing to the lower transition energy. However, as the field frequency increases, $\sigma_y^{(3)}(\omega)$ falls more rapidly

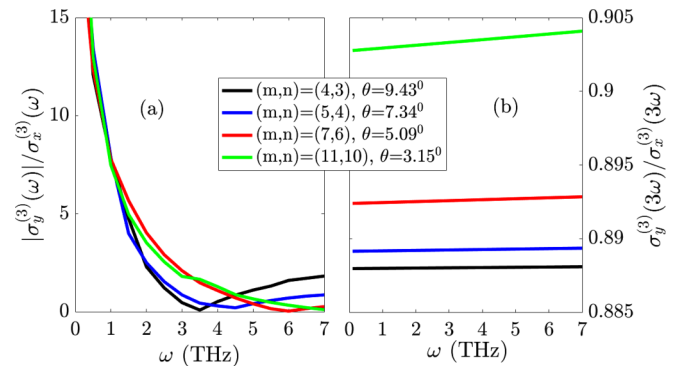


FIG. 6. Anisotropy of the third-order conductivity $T = 300$ K and $\mu = 0.1$ eV. (a) For two-photon absorption, one-photon emission processes. (b) For three-photon absorption processes.

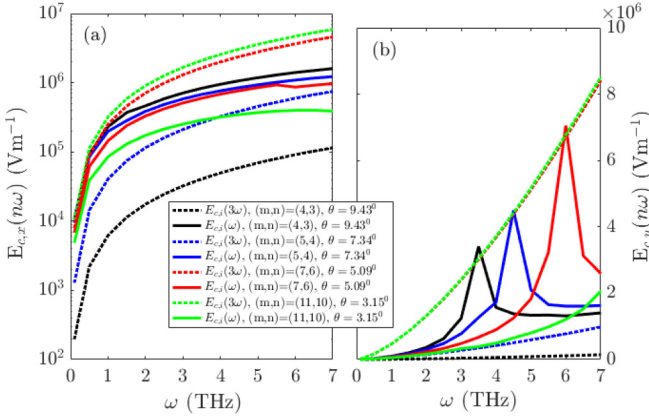


FIG. 7. Critical field in the THz region for $T = 300$ K, $\mu = 0.1$ eV, and different twist angles. (a) In the x direction. (b) In the y direction.

as available carriers begin to disproportionately participate in single-photon processes until $\sigma_y^{(3)}(\omega)$ becomes negative and the defocusing discontinuity occurs. This phenomenon is magnified at larger twist angles where the interlayer response is mitigated. Figure 6(b) shows the frequency-tripled response in the x direction remains dominant by $\approx 10\%$ over the entire frequency domain. We attribute this feature to carriers selectively participating in lower transition energy processes more readily in the y direction, where the interlayer response is greater. Our attribution of most nonlinear anisotropy features to the interlayer response is consistent with findings in the NIR range where, relative to the overall response, the interlayer response at the third harmonic is 5 times larger than at the first harmonic [55].

C. Critical field

Since the first-order current scales with E/ω^2 and the third-order current scales with E^3/ω^6 at sufficiently high fields or low frequencies, the nonlinear current will be of considerable magnitude. To quantify when this occurs, we define the critical field as the electric field required to make the first- and third-order current equal in magnitude,

$$E_{c,v} = \sqrt{\left| \frac{\sigma_v^{(1)}}{\sigma_v^{(3)}} \right|}.$$

Figure 7 shows that the magnitude of the critical field encompasses $E_{c,x} \in [10^2 - 10^7]$ V/m over the frequency range surveyed for different twist angles. For THz frequencies SLG lies well within the lower bound of this range with $E_c(\omega) \in [1600 - 2600]$ V/m and $E_c(3\omega) \in [1700 - 2700]$ V/m [16], and BLG lies more in the center with $E_c(\omega) \in [6 \times 10^4, 1.5 \times 10^6]$ V/m and $E_c(3\omega) \in [1.1 \times 10^5, 2 \times 10^6]$ V/m [18]. Although our model relies on fundamentally different assumptions, an extrapolation of our results into the NIR frequency region for a large twist angle of 21.8° falls just below the equivalent $E_{c,x} = 10^8$ V/m value in [55].

In Fig. 7(a), the increased robustness of the twist angle and frequency for $E_{c,x}(\omega)$ is consistent with the analysis of $\sigma_x^{(3)}(\omega)$. A salient point for the larger twist angles is that the critical field is up to an order of magnitude smaller for

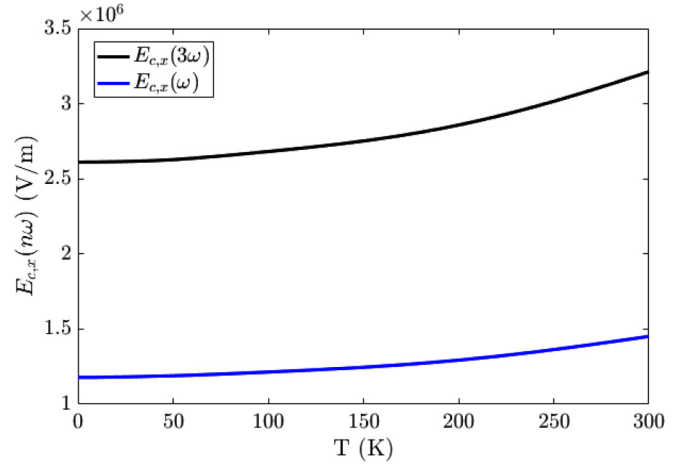


FIG. 8. Temperature dependence of the critical field $E_{c,x}$ for $(m, n) = (7, 6)$, $\theta = 5.09^\circ$, $\omega = 1$ THz, and $\mu = 0.1$ eV.

the frequency-tripled component at lower THz frequencies: $E_{c,x}(3\omega) \approx 10^4$ for $\theta = 9.43^\circ$. This is not the case for BLG, where $E_c(3\omega) > E_c(\omega)$ over the entire THz range [18] as per the frequency dependence of $\sigma^{(3)}$. The main difference between the frequency dependences of the critical fields in the x and y directions is the peaked structure of $E_{c,y}(\omega)$ shown in Fig. 7(b). This feature is a remnant of the change in polarity of $\sigma_y^{(3)}(\omega)$ and as such occurs at higher frequencies for smaller twist angles.

Owing to the different harmonic processes present within the third-order current, the distribution function is modified, and the temperature dependence is no longer straightforwardly controlled by $N_F(\epsilon, \mu)$. To capture this nontrivial temperature dependence Fig. 8 is produced.

The nonlinear response of TBG is found to be less sensitive to thermal fluctuations when compared to SLG. Figure 8 shows that $E_{c,x}(3\omega)$ increases $\approx 25\%$ from 0 to 300 K, while $E_{c,x}(\omega)$ increases $\approx 20.8\%$ over the same range. These values are in comparison to $E_c(3\omega)$ increasing $\approx 32.3\%$ and $E_c(\omega)$ increasing $\approx 46.9\%$ in SLG, while $E_c(3\omega)$ decreases $\approx 45\%$ and $E_c(\omega)$ decreases $\approx 29\%$ over the same temperature range for $\omega = 1$ THz [16]. For SLG at 0 K $E_{c,x}(3\omega)$ is $\approx 6.25\%$ larger than $E_{c,x}(\omega)$, but $E_{c,x}(\omega)$ increases faster with temperature, producing a crossover point at ≈ 180 K, where $E_{c,x}(3\omega) < E_{c,x}(\omega)$. Such a feature is absent from both TBG and BLG. In this way thermal tunability for a frequency-tripled response is sacrificed for robustness. In TBG $E_{c,x}(3\omega)$ is $\approx 116\%$ larger than $E_{c,x}(\omega)$ at 0 K for $\theta = 5.09^\circ$ and increases more rapidly over $T \in [0, 300]$ K, while in BLG $E_c(3\omega)$ is $\approx 83\%$ larger than $E_c(\omega)$ at 0 K and decreases more rapidly to end $\approx 29\%$ larger at 300 K. The fact that E_c increases with temperature regardless of twist angle in TBG can only be attributed to the twist-induced saddle point producing not only a more frequency sensitive nonlinear current but a more temperature sensitive nonlinear current as well.

IV. CONCLUSION

For a low-energy effective two-band model we have employed a quantum mechanical formalism to recursively

determine wave function components that couple charge carriers in TBG to successive orders of a spatially constant electric field. The wave functions were used to calculate the linear and third-order (lowest nonlinear order) current responses in both the x and y directions (parallel to the direction of the applied field) and their dependence on temperature, Fermi level, and twist angle. The validity of this model relies on $\omega < 2.13 \times 10^{14}$ Hz so that carriers from the innermost conduction and valence bands participate in interband transitions. Furthermore, the region of twist angles sampled was $3^\circ \leq \theta \leq 10^\circ$, which is large enough to avoid localization effects and small enough for the interlayer hopping matrix to resemble Bernal bilayer graphene [43,47,51,63].

The most salient feature of the first-order conductivity is its twist angle dependence. It was shown that as $\theta = 3^\circ \rightarrow 10^\circ$, the first-order conductivity increases by almost two orders of magnitude in the THz range. This is attributed to the BZ enlargement (decreased unit cell in coordinate space) for larger twist angles and persists for the nonlinear third-order conductivity. The drastic change in optical conductivities by twisting opens the possibility for use of TBG in optotwistronics (also known as twistronics). With magnitudes two orders smaller than comparative studies on the nonlinear conductance of bilayer graphene without a twist [18], TBG was found to sacrifice nonlinear activity for high tunability with twist angle, a high degree of anisotropy, and a larger robustness to temperature fluctuations. This decrease in nonlinearity yields a critical field only one order of magnitude larger than BLG

at $\approx 10^5$ V/m. Given this is still a practically accessible field and similar to other materials such as nodal semimetals [67] and α - T_3 lattices [68], TBG should be considered a candidate for THz optics and photonics devices such as THz emitters, detectors, and mixers. The most desirable feature uncovered in this paper the dominance of the frequency-tripled nonlinear conductivity for larger twist angles, producing low critical fields of the order of 10^4 V/m at room temperature. This phenomenon is imperative for THz up-conversion devices by using another emitter at 1/3 of the desired frequency.

As a final remark we comment on our omission of phonon excitation and relaxation phenomena. The dominant electron-phonon coupling mode is the longitudinal acoustic (LA) mode at room temperature [70,71]. Given LA phonons have a velocity of $\approx 2 \times 10^4$ m/s and the carriers we considered reside close to the $\mathbf{K}_{(\theta)}$ points, where their velocity $\approx v_F$, the probabilities of single-phonon emission and multiple-phonon excitation are negligible. Since our model is designed to capture the current produced by low-energy carriers residing near the Dirac points, relaxation due to impurity scattering should become relevant only for driving fields of magnitude larger than megavolts per centimeter [55,72,73].

ACKNOWLEDGMENT

This research has been supported by the Australian Research Council (Grant No. DP210101436).

- [1] Z. Yan, Z. Peng, Z. Sun, J. Yao, Y. Zhu, Z. Liu, P. M. Ajayan, and J. M. Tour, *ACS Nano* **5**, 8187 (2011).
- [2] L. Xie, H. Wang, C. Jin, X. Wang, L. Jiao, K. Suenaga, and H. Dai, *J. Am. Chem. Soc.* **133**, 10394 (2011).
- [3] R. Zhao, Y. Zhang, T. Gao, Y. Gao, N. Liu, L. Fu, and Z. Liu, *Nano Res.* **4**, 712 (2011).
- [4] C. Berger, Z. Song, X. Li, X. Wu, N. Brown, C. Naud, D. Mayou, T. Li, J. Hass, A. N. Marchenkov, and E. H. Conrad, *Science* **312**, 1191 (2006).
- [5] Z. Ni, Y. Wang, T. Yu, Y. You, and Z. Shen, *Phys. Rev. B* **77**, 235403 (2008).
- [6] V. P. Gusynin, S. G. Sharapov, and J. P. Carbotte, *Phys. Rev. Lett.* **96**, 256802 (2006).
- [7] A. B. Kuzmenko, E. van Heumen, F. Carbone, and D. van Der Marel, *Phys. Rev. Lett.* **100**, 117401 (2008).
- [8] R. R. Nair, P. Blake, A. N. Grigorenko, K. S. Novoselov, T. J. Booth, T. Stauber, N. M. R. Peres, and A. K. Geim, *Science* **320**, 1308 (2008).
- [9] C. Zhang, L. Chen, and Z. Ma, *Phys. Rev. B* **77**, 241402(R) (2008).
- [10] K. S. Novoselov, A. K. Geim, S. V. Morozov, D. Jiang, M. I. Katsnelson, I. V. Grigorieva, S. V. Dubonos, and A. A. Firsov, *Nature (London)* **438**, 197 (2005).
- [11] Y. Zhang, Y. W. Tan, H. L. Stormer, and P. Kim, *Nature (London)* **438**, 201 (2005).
- [12] H. Suzuura and T. Ando, *J. Phys. Soc. Jpn.* **72**, 69 (2003).
- [13] S. V. Morozov, K. S. Novoselov, M. I. Katsnelson, F. Schedin, L. A. Ponomarenko, D. Jiang, and A. K. Geim, *Phys. Rev. Lett.* **97**, 016801 (2006).
- [14] J. Liu, A. R. Wright, C. Zhang, and Z. Ma, *Appl. Phys. Lett.* **93**, 041106 (2008).
- [15] S. A. Mikhailov and K. Ziegler, *J. Phys.: Condens. Matter* **20**, 384204 (2008).
- [16] A. R. Wright, X. G. Xu, J. C. Cao, and C. Zhang, *Appl. Phys. Lett.* **95**, 072101 (2009).
- [17] A. R. Wright, F. Liu, and C. Zhang, *Nanotechnology* **20**, 405203 (2009).
- [18] Y. S. Ang, S. Sultan, and C. Zhang, *Appl. Phys. Lett.* **97**, 243110 (2010).
- [19] C. J. Tabert and E. J. Nicol, *Phys. Rev. B* **86**, 075439 (2012).
- [20] L. Ju, L. Wang, X. Li, S. Moon, M. Ozerov, Z. Lu, T. Taniguchi, K. Watanabe, E. Mueller, F. Zhang, D. Smirnov, F. Rana, and P. L. McEuen, *Nat. Commun.* **11**, 2941 (2020).
- [21] I. Crassee, J. Levallois, D. van Der Marel, A. L. Walter, Th. Seyller, and A. B. Kuzmenko, *Phys. Rev. B* **84**, 035103 (2011).
- [22] E. McCann and V. I. Fal'ko, *Phys. Rev. Lett.* **96**, 086805 (2006).
- [23] T. Ohta, A. Bostwick, T. Seyller, K. Horn, and E. Rotenberg, *Science* **313**, 951 (2006).
- [24] E. V. Castro, K. S. Novoselov, S. V. Morozov, N. M. R. Peres, J. M. B. Lopes Dos Santos, J. Nilsson, F. Guinea, A. K. Geim, and A. H. Castro Neto, *Phys. Rev. Lett.* **99**, 216802 (2007).
- [25] Z. Q. Li, E. A. Henriksen, Z. Jiang, Z. Hao, M. C. Martin, P. Kim, H. L. Stormer, and D. N. Basov, *Phys. Rev. Lett.* **102**, 037403 (2009).
- [26] H. Min and A. H. MacDonald, *Phys. Rev. B* **77**, 155416 (2008).
- [27] J. Hass, F. Varchon, J. E. Millan-Otoya, M. Sprinkle, N. Sharma, W. A. de Heer, C. Berger, P. N. First, L. Magaud, and E. H. Conrad, *Phys. Rev. Lett.* **100**, 125504 (2008).

- [28] E. Suárez Morell, J. D. Correa, P. Vargas, M. Pacheco, and Z. Barticevic, *Phys. Rev. B* **82**, 121407(R) (2010).
- [29] G. Trambly de Laissardière, D. Mayou, and L. Magaud, *Nano Lett.* **10**, 804 (2010).
- [30] R. Bistritzer and A. H. MacDonald, *Proc. Natl. Acad. Sci. USA* **108**, 12233 (2011).
- [31] Z. Ni, L. Liu, Y. Wang, Z. Zheng, L. J. Li, T. Yu, and Z. Shen, *Phys. Rev. B* **80**, 125404 (2009).
- [32] A. Righi, S. D. Costa, H. Chacham, C. Fantini, P. Venezuela, C. Magnuson, L. Colombo, W. S. Bacsá, R. S. Ruoff, and M. A. Pimenta, *Phys. Rev. B* **84**, 241409(R) (2011).
- [33] K. Sato, R. Saito, C. Cong, T. Yu, and M. S. Dresselhaus, *Phys. Rev. B* **86**, 125414 (2012).
- [34] T. Ohta, T. E. Beechem, J. T. Robinson, and G. L. Kellogg, *Phys. Rev. B* **85**, 075415 (2012).
- [35] Y. Wang, Z. Ni, L. Liu, Y. Liu, C. Cong, T. Yu, X. Wang, D. Shen, and Z. Shen, *ACS Nano* **4**, 4074 (2010).
- [36] X. Zou, J. Shang, J. Leaw, Z. Luo, L. Luo, C. La-o-vorakiat, L. Cheng, S. A. Cheong, H. Su, J. X. Zhu, Y. Liu, K. P. Loh, A. H. Castro Neto, T. Yu, and E. E. M. Chia, *Phys. Rev. Lett.* **110**, 067401 (2013).
- [37] J. Liu and X. Dai, *njp Comput. Mater.* **6**, 57 (2020).
- [38] P. Moon and M. Koshino, *Phys. Rev. B* **85**, 195458 (2012).
- [39] T. Stauber, P. San-Jose, and L. Brey, *New J. Phys.* **15**, 113050 (2013).
- [40] T. Stauber, T. Low, and G. Gómez-Santos, *Phys. Rev. B* **98**, 195414 (2018).
- [41] T. Stauber, T. Low, and G. Gómez-Santos, *Phys. Rev. Lett.* **120**, 046801 (2018).
- [42] X. Lin, Z. Liu, T. Stauber, G. Gómez-Santos, F. Gao, H. Chen, B. Zhang, and T. Low, *Phys. Rev. Lett.* **125**, 077401 (2020).
- [43] R. de Gail, M. O. Goerbig, F. Guinea, G. Montambaux, and A. H. Castro Neto, *Phys. Rev. B* **84**, 045436 (2011).
- [44] H. C. Po, L. Zou, A. Vishwanath, and T. Senthil, *Phys. Rev. X* **8**, 031089 (2018).
- [45] M. Otteneder, S. Hubmann, X. Lu, D. A. Kozlov, L. E. Golub, K. Watanabe, T. Taniguchi, D. K. Efetov, and S. D. Ganichev, *Nano Lett.* **20**, 7152 (2020).
- [46] Y. Gao, Y. Zhang, and D. Xiao, *Phys. Rev. Lett.* **124**, 077401 (2020).
- [47] M. Y. Choi, Y. H. Hyun, and Y. Kim, *Phys. Rev. B* **84**, 195437 (2011).
- [48] C. T. Ellis, A. V. Stier, M. H. Kim, J. G. Tischler, E. R. Glaser, R. L. Myers-Ward, J. L. Tedesco, C. R. Eddy, D. K. Gaskill, and J. Cerne, *Sci. Rep.* **3**, 3143 (2013).
- [49] O. V. Kotov and Y. E. Lozovik, *Phys. Rev. B* **96**, 235403 (2017).
- [50] M. He, H. Qi, Y. Ren, Y. Zhao, and M. Antezza, *Int. J. Heat Mass Transfer* **150**, 119305 (2020).
- [51] C. J. Tabert and E. J. Nicol, *Phys. Rev. B* **87**, 121402(R) (2013).
- [52] L. Wen, Z. Li, and Y. He, *Chin. Phys. B* **30**, 017303 (2021).
- [53] P. Moon and M. Koshino, *Phys. Rev. B* **87**, 205404 (2013).
- [54] R. McGouran, I. Al-Naib, and M. M. Dignam, *Phys. Rev. B* **94**, 235402 (2016).
- [55] T. N. Ikeda, *Phys. Rev. Research* **2**, 032015(R) (2020).
- [56] C. P. Zhang, J. Xiao, B. T. Zhou, J. X. Hu, Y. M. Xie, B. Yan, and K. T. Law, [arXiv:2010.08333](https://arxiv.org/abs/2010.08333).
- [57] F. Yang, W. Song, F. Meng, F. Luo, S. Lou, S. Lin, Z. Gong, J. Cao, E. S. Barnard, E. Chan, and L. Yang, *Matter* **3**, 1361 (2020).
- [58] V. Kumar, U. Kumar, and G. S. Setlur, *Pramana* **83**, 597 (2014).
- [59] E. J. Mele, *Phys. Rev. B* **81**, 161405(R) (2010).
- [60] E. J. Mele, *J. Phys. D* **45**, 154004 (2012).
- [61] Y. K. Huang, S. C. Chen, Y. H. Ho, C. Y. Lin, and M. F. Lin, *Sci. Rep.* **4**, 7509 (2014).
- [62] S. Shallcross, S. Sharma, E. Kandelaki, and O. A. Pankratov, *Phys. Rev. B* **81**, 165105 (2010).
- [63] J. M. B. Lopes dos Santos, N. M. R. Peres, and A. H. Castro Neto, *Phys. Rev. Lett.* **99**, 256802 (2007).
- [64] J. M. B. Lopes dos Santos, N. M. R. Peres, and A. H. Castro Neto, *Phys. Rev. B* **86**, 155449 (2012).
- [65] S. Shallcross, S. Sharma, and O. A. Pankratov, *Phys. Rev. Lett.* **101**, 056803 (2008).
- [66] R. Bistritzer and A. H. MacDonald, *Phys. Rev. B* **81**, 245412 (2010).
- [67] J. W. Zuber, T. Zhao, S. Gong, M. Hu, R. B. Zhong, C. Zhang, and S. G. Liu, *Phys. Rev. B* **101**, 085307 (2020).
- [68] L. Chen, J. W. Zuber, Z. Ma, and C. Zhang, *Phys. Rev. B* **100**, 035440 (2019).
- [69] S. Shareef, Y. S. Ang, and C. Zhang, *J. Opt. Soc. Am. B* **29**, 274 (2012).
- [70] E. H. Hwang and S. D. Sarma, *Phys. Rev. B* **77**, 115449 (2008).
- [71] A. I. Cocemasov, D. L. Nika, and A. A. Balandin, *Phys. Rev. B* **88**, 035428 (2013).
- [72] G. Orlando, C. M. Wang, T. S. Ho, and S. I. Chu, *J. Opt. Soc. Am. B* **35**, 680 (2018).
- [73] K. Chinzei and T. N. Ikeda, *Phys. Rev. Research* **2**, 013033 (2020).